

Hallucinating Statistical Moment and Subspace Descriptors from Object and Saliency Detectors for Action Recognition

Lei Wang^{*,1,2} Piotr Koniusz^{*,1,2}

¹Data61/CSIRO, ²Australian National University
 firstname.lastname@{data61.csiro.au¹, anu.edu.au²}

Abstract

In this paper, we build on a deep translational action recognition network which takes RGB frames as input to learn to predict both action concepts and auxiliary supervisory feature descriptors e.g., Optical Flow Features and/or Improved Dense Trajectory descriptors. The translation is performed by so-called hallucination streams trained to predict auxiliary cues which are simultaneously fed into classification layers, and then hallucinated for free at the testing stage to boost recognition. In this paper, we design and hallucinate two descriptors, one leveraging four popular object detectors applied to training videos, and the other leveraging image- and video-level saliency detectors. The first descriptor encodes the detector- and ImageNet-wise class prediction scores, confidence scores, and spatial locations of bounding boxes and frame indexes to capture the spatio-temporal distribution of features per video. Another descriptor encodes spatio-angular gradient distributions of saliency maps and intensity patterns. Inspired by the characteristic function of the probability distribution, we capture four statistical moments on the above intermediate descriptors. As numbers of coefficients in the mean, covariance, coskewness and cokurtosis grow linearly, quadratically, cubically and quartically w.r.t. the dimension of feature vectors, we describe the covariance matrix by its leading n' eigenvectors (so-called subspace) and we capture skewness/kurtosis rather than costly coskewness/cokurtosis. We obtain state of the art on three popular datasets.

1. Introduction

Action Recognition (AR) approaches have progressed from hand-crafted video representations [13, 60, 35, 71, 72, 73] to approaches based on Convolutional Neural Networks (CNN) [62, 67, 18, 4]. The two-stream networks [62], 3D spatio-temporal features [67], spatio-temporal ResNet

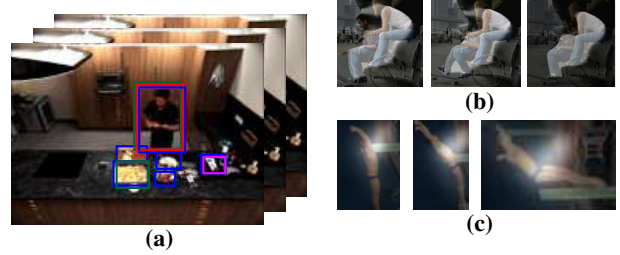


Figure 1: We use detectors and saliency in hallucination descriptors. Figure 1a shows bounding boxes from four detectors. The faster R-CNN detector with ResNet101 focuses on human-centric actions such as *stand*, *watch*, *talk*, etc. The other three detectors discover objects e.g., *oven*, *sink*, *clock*, etc. Figure 1b shows that the MNL saliency detector focuses on spatial regions. Figure 1c shows ACLNet saliency detector discovers motion regions.

model [18] and the new Inflated 3D (I3D) convolutions network pre-trained on Kinetics-400 [4]. Often, AR networks learn representations on the RGB and optical flow frames, and they benefit from a late fusion (ahead of the classifier level) with low-level representations such as Improved Dense Trajectory (IDT) descriptors [73] due to their highly complementary nature [21, 7, 8, 74, 9].

A recent deep translational AR pipeline [75] (we call it DEEP-HAL) has successfully shown that IDT descriptors encoded with Bag-of-Words (BoW) [63, 11] and Fisher Vectors (FV) [50, 51] can be learnt by so-called hallucination streams and generated at the testing stage to boost results beyond a naive fusion of modalities. Furthermore, both DEEP-HAL and approach [66] have demonstrated that even optical flow frames encoded by a deep network can be learnt by another network trained on RGB frames only, thus pointing that training RGB and optical flow streams of in the I3D network simultaneously is perhaps somewhat redundant. DEEP-HAL [75] have attained state-of-the-art results on several AR benchmarks by simply learning to hallucinate IDT-based BoW/FV and Optical Flow Features (OFF) from a single RGB stream I3D network.

DEEP-HAL opens up an exciting opportunity to investigate what other representations can co-regularize/self-supervise an I3D network for AR with the goal of learning to hallucinate costly representations at the training stage and simply leveraging outputs of hallucination streams at the

*Both authors contributed equally. Please respect the authors' efforts by not copying/plagiarizing bits and pieces of this work for your own gain (we will vigorously pursue dishonest authors). If you find anything inspiring in this work, be kind enough to cite it thus showing you care for the CV community.

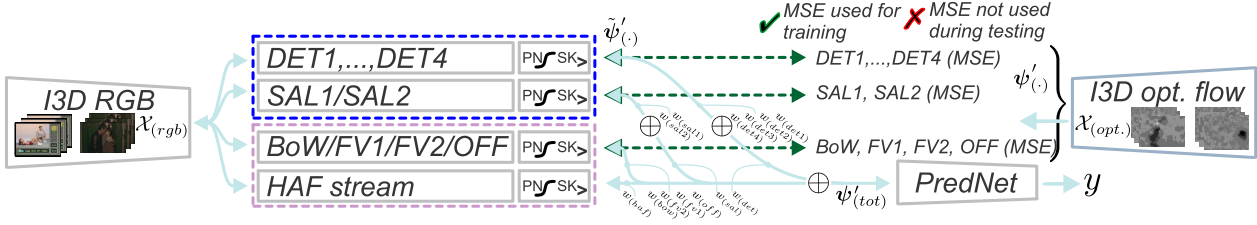


Figure 2: We build on DEEP-HAL [75] which includes I3D RGB and Optical Flow networks (the latter net. is used only during training). Specifically, we remove the prediction and the last 1D conv. layers from I3D RGB and optical flow streams, we feed the 1024×7 feature representations $\mathcal{X}_{(rgb)}$ into *Bag-of-Words (BoW)*, *Fisher Vector (FV)*, the *Optical Flow Features (OFF)* and the *High Abstraction Features (HAF)* streams (dashed red) followed by the *Power Normalization (PN)* and *Sketching (SK)* blocks, the latter addition departs from DEEP-HAL. The OFF stream is supervised by $\mathcal{X}_{(opt.)}$. Moreover, we introduce *DET1*, ..., *DET4*, *SAL1* and *SAL2* streams corresponding to our detector- and saliency-based descriptors (dashed blue). The resulting feature vectors $\tilde{\psi}'_{(\cdot)}$, where (\cdot) denotes the stream name *e.g.*, $(det1)$, ..., $(det2)$ etc., are reweighted by corresponding weights $w_{(\cdot)}$ and aggregated (sum) by \oplus . All $\tilde{\psi}'_{(\cdot)}$ are reweighted, aggregated (sum) and fed to *Prediction Network (PredNet)*. By \checkmark , we indicate that the Mean Square Error (MSE) losses are used during training (and the class. loss) to supervise all streams outputting $\tilde{\psi}'_{(\cdot)}$ by the ground-truth $\psi'_{(\cdot)}$. By \times , we indicate that the MSE losses are switched off for testing and $\tilde{\psi}'_{(\cdot)}$ are hallucinated/fed into PredNet to obtain labels y .

testing time. We leverage recent advances in deep translational AR pipelines. We build on DEEP-HAL which already includes IDT-based BoW/FV and OFF streams. However, we investigate the self-supervisory ability of object/saliency detectors in hallucination-based AR pipelines.

In this paper, we design and hallucinate two kinds of descriptors such as Object Detection Features (ODF) and Saliency Detection Features (SDF). The ODF descriptor leverages faster R-CNN detector [55] based on backbones such as (i) Inception V2 [65], (ii) Inception ResNet V2 [64], (iii) ResNet101 [28] and (iv) NASNet [85]. We note that the Inception V2, Inception ResNet V2 and NASNet are pre-trained on the COCO dataset [45], which contains 91 object classes; whereas the ResNet101 is pre-trained on the AVA v2.1 dataset [25] that contains 80 different human actions. The above detector models are applied to training videos with the goal of identifying humans and objects which are relevant to the task of action recognition. Such detected objects together with their relevance and class labels summarized with our descriptor are likely going to force the AR pipeline to focus on these semantically important regions correlating with relevant actions. Figure 1a illustrates a few of bounding boxes detected by these four detectors.

The SDF leverages image- and video-level saliency detectors such as MNL [83] and ACLNet [82] with the goal of identifying salient regions correlating with the human gaze in spatial and temporal sense. Both such saliency maps extracted from training videos and summarized by our descriptor are expected to help the AR pipeline learn spatial and temporal regions correlating with relevant actions. Figures 1b and 1c illustrate saliency maps extracted with region- and temporally-wise saliency detectors.

IDT descriptors are fused with the majority of the modern CNN-based approaches [21, 7, 8, 74, 9] at the classifier level for the best performance while DEEP-HAL [75]

learns to hallucinate them and simultaneously feeds them into the classification branch called PredNet. In this paper, we go further and prepare two compact descriptors, ODF and SDF, and hallucinate them within DEEP-HAL. We equip each hallucination branch with a weighting mechanism adjusted per epoch to attain the best results. Figure 2 illustrates DEEP-HAL at the conceptual level.

For ODF descriptors, per bounding box per frame, we concatenate together (i) the one-hot detection and (ii) ImageNet [58] scores, (iii) embedded confidence scores, (iv) embedded bounding box coordinates, and (v) embedded normalized frame index. For all bounding boxes, we stack such features into a matrix. Inspired by the characteristic function of the probability density fun., we extract the mean, leading eigenvectors of covariance, skewness and kurtosis. For SDF descriptors, per frame, we encode saliency via (i) kernelized descriptor on spatio-angular gradient distributions of saliency maps and (ii) intensity patterns. We obtain an ODF per detector and an SDF per saliency detector. Our contributions are as follows:

- i. We propose to utilize the object and human detectors to enhance the performance of AR pipelines.
- ii. We design two types of compact descriptors called Object Detection Features and Saliency Detection Features for the use in AR pipelines. These descriptors are statistically motivated high-order representations.
- iii. We build on the recent DEEP-HAL [75] pipeline, we introduce a weight learning mechanism for hallucinated feature vectors, and ODF and SDF are hallucinated which leads to the state-of-the-art performance.

2. Related Work

Below, we describe handcrafted spatio-temporal video descriptors, their encoding strategies and the optical flow used by DEEP-HAL [75]. We also describe deep learning

pipelines for video classification. Finally, we discuss the object category and human detectors followed by the spatial and temporal saliency detectors used in this work.

Early video descriptors. Early AR used on spatio-temporal interest point detectors [43, 14, 5, 79, 44, 71] and spatio-temporal descriptors [13, 60, 68, 71, 72, 73] which capture various appearance and motion statistics.

As spatio-temporal interest point detectors is unable to capture long-term motion patterns, a Dense Trajectory (DT) [71] approach densely samples feature points in each frame to track them in the video (via optical flow). Then, multiple descriptors are extracted along trajectories to capture shape, appearance and motion cues. As DT cannot compensate for the camera motion, the IDT [73, 72] estimates the camera motion to remove the global background motion. IDT also removes inconsistent matches via a human detector. For spatio-temporal descriptors, IDT employs HOG [22], HOF [13] and MBH [72]. HOG [22] contains statistics of the amplitude of image gradients w.r.t. the gradient orientation. Thus, it captures the static appearance cues while its close cousin, HOG-3D [35], is designed for spatio-temporal interest points. In contrast, HOF [13] captures histograms of optical flow while MBH [72] captures derivatives of the optical flow, thus it is highly resilient to the global camera motion whose cues cancel out due to derivatives. Thus, HOF and MBH contain the zero- and first-order optical flow statistics. Other spatio-temporal descriptors include SIFT3D [60], SURF3D [79] and LTP [81].

In this work, we use the DEEP-HAL [75] setup. We encode HOG, HOF, and MBH descr. on the Improved Dense Trajectories [71, 7, 9] via BoW [63, 11] and FV [50, 51].

BoW/FV encoding. BoW [63, 11], a global image representation uses k-means vocabulary to which local descriptors are assigned. Variants include Soft Assignment (SA) [69, 37] and Localized Soft Assignment (LcSA) [46, 40].

As we use DEEP-HAL [75], we use BoW [11] with Power Normalization [40], and FV [50, 51] which capture first- and second-order statistics of local descriptors assigned to GMM clusters. DEEP-HAL [75] setup describes how to obtain the BoW/FV global descriptors.

Optical flow. A key component of modern AR pipelines [62, 4, 20, 74], older optical flow methods cope with small displacements [29, 49] while newer methods cope with larger displacements *e.g.*, Large Displacement Optical Flow (LDOF) [3]. Recent methods use non-rigid descriptor or segment matching [78, 2], or edge-preserving interpolation [56]. As use the DEEP-HAL [75], we also use LDOF [49].

Object detectors. Widely used in computer vision [12, 24, 54], early detectors used handcrafted HOG and/or opt. flow descriptors [12, 13]. Modern deep learning methods include Region-based Convolutional Neural Networks (R-CNN) [24], its faster variants [23, 55], its mask-based variants [27], and YOLO [54], YOLO v2, YOLO v3 *etc.*, which

use a single network for efficiency.

In this paper, we use the faster R-CNN detector [55] with backbones such as (i) Inception V2 [65], (ii) Inception ResNet V2 [64], (iii) ResNet101 [28] and (iv) NASNet [85]. As the Inception V2, Inception ResNet V2 and NASNet are pre-trained on the COCO dataset [45], they detect from 91 object classes good at summarizing *e.g.*, indoor environments and helping us associate the scene context with actions. The ResNet101 model is pre-trained on the AVA v2.1 dataset [25] with 80 different human actions, thus directly helping human-centric action recognition problems.

In addition to the classification scores from detectors, we described each bounding box with ImageNet [58] scores from pre-trained Inception ResNet V2 [64].

Saliency detectors. Image regions correlating with human visual attention are detected by saliency detectors in the form of saliency maps. Conventional saliency detectors underperform on complex scenes due to human-defined priors [84]. Deep saliency models [76, 30] outperform conventional saliency detectors but they require laborious pixel-wise labels. Recent popular models include MNL [83] (weakly-supervised model), RFCN [76] (a fully-supervised model) and a cheap non-CNN Robust Background Detector (RBD) [84] (see survey [1] for more details).

For the spatial saliency, we use MNL [83] trained on multiple noisy labels from weak and noisy unsupervised handcrafted saliency methods. For temporal saliency, we use ACLNet [82], a CNN-LSTM based mechanism.

Deep learning AR. Early AR CNN models use frame-wise features and average pooling [34] discarding the temporal order. Thus, frame-wise CNN scores were fed to LSTMs [15] while the two-stream networks [62] compute representations per RGB frame and per 10 stacked optical flow frames. Finally, spatio-temporal 3D CNN filters [33, 67, 18, 70] model spatio-temporal patterns.

As two-stream networks [62] discard the temporal order, rank pooling [20, 21, 8, 74, 8, 74] and higher-order pooling [7, 36, 39, 16] are popular. A recent I3D model [4] ‘inflates’ 2D CNN filters pre-trained on ImageNet to spatio-temporal 3D filters, and implements temporal pooling. We use DEEP-HAL [75] which employs a 1D convolution for temporal pooling on the I3D network, but our proposed object and saliency descriptors are independent of the backbone—we are concerned with the design/ability of ODF/SDF to co-regularize DEEP-HAL for the best performance.

Power Normalization. For BoW/FV and CNN-based streams, the so-called burstiness defined as ‘*the property that a given visual element appears more times in an image than a statistically independent model would predict*’ [32] has to be tackled. Thus, we employ Power Normalization [40, 38, 39, 41] which suppresses the burstiness via the so-called MaxExp pooling [40] given in Section 3.

3. Background

In what follows, we present Power Normalization [40, 39], count sketches [77], and the RBF feature maps which we use in our pipeline with the goal of the burstiness and dimensionality reduction, and Cartesian coordinate/frame index encoding. Firstly, we explain our notations.

Notations. We use boldface uppercase letters to express matrices *e.g.*, \mathbf{M}, \mathbf{P} , regular uppercase letters with a subscript to express matrix elements *e.g.*, P_{ij} is the $(i, j)^{\text{th}}$ element of \mathbf{P} , boldface lowercase letters to express vectors, *e.g.* \mathbf{x}, ϕ, ψ , and regular lowercase letters to denote scalars. Vectors can be numbered *e.g.*, \mathbf{x}_n while regular lowercase letters with a subscript express an element of vector *e.g.*, v_{x_i} is the i^{th} element of \mathbf{x} . Operators ‘;’ and ‘,’ concatenate vectors along the first and second mode, *respe.*, $\odot_{i \in \mathcal{I}_K} \mathbf{v}_i = [\mathbf{v}_1; \dots; \mathbf{v}_K]$ and $\odot_{i \in \mathcal{I}_K}^2 \mathbf{v}_i = [\mathbf{v}_1, \dots, \mathbf{v}_K]$ concatenate a group of vectors in the first and second mode, *resp.*, \oplus denotes the aggregation (sum) while \mathcal{I}_d denotes an index set of integers $\{1, \dots, d\}$.

3.1. Power Normalization

Proposition 1. *Sigmoid (SigmE), a Max-pooling approximation [41], is an extension of the MaxExp operator defined as $g(\psi, \eta) = 1 - (1 - \psi)^\eta$ for $\eta > 1$ to the operator with a smooth derivative, a response defined for real-valued ψ (rather than $\psi \geq 0$), a parameter η' and a small const. ϵ' :*

$$g(\psi, \eta') = \frac{2}{1 + e^{-\eta' \psi / (\|\psi\|_2 + \epsilon')}} - 1. \quad (1)$$

Proof. See papers [40, 41] for extensive considerations. \square

As papers [40, 75] show that various pooling operators perform similarly, we equip our hallucination streams with SigmE followed by count sketching described below.

3.2. Count Sketches

Sketching vectors by the count sketch [10, 77] is used for their dimensionality reduction which we use in this paper.

Proposition 2. *Let d and d' denote the dimensionality of the input and sketched output vectors, respectively. Let vector $\mathbf{h} \in \mathcal{I}_{d'}^d$ contain d uniformly drawn integer numbers from $\{1, \dots, d'\}$ and vector $\mathbf{s} \in \{-1, 1\}^d$ contain d uniformly drawn values from $\{-1, 1\}$. Then, the sketch projection matrix $\mathbf{P} \in \{-1, 0, 1\}^{d' \times d}$ becomes:*

$$P_{ij} = \begin{cases} s_i & \text{if } h_i = j, \\ 0 & \text{otherwise,} \end{cases} \quad (2)$$

and the sketch projection $p: \mathbb{R}^d \rightarrow \mathbb{R}^{d'}$ is a linear operation given as $p(\psi) = \mathbf{P}\psi$ (or $p(\psi; \mathbf{P}) = \mathbf{P}\psi$ to highlight \mathbf{P}).

Proof. It directly follows from the definition of the count sketch *e.g.*, see Definition 1 [77]. \square

Remark 1. *Count sketches are unbiased estimators: $\mathbb{E}_{\mathbf{h}, \mathbf{s}}(p(\psi, \mathbf{P}(\mathbf{h}, \mathbf{s})), p(\psi', \mathbf{P}(\mathbf{h}, \mathbf{s}))) = \langle \psi, \psi' \rangle$. As variance $\mathbb{V}_{\mathbf{h}, \mathbf{s}}(p(\psi), p(\psi')) \leq \frac{1}{d'} \left(\langle \psi, \psi' \rangle^2 + \|\psi\|_2^2 \|\psi'\|_2^2 \right)$, we larger sketches are less noisy. Thus, for every modality we compress, we use a separate sketch matrix \mathbf{P} .*

Proof. For the first and second property, see Appendix A of paper [77] and Lemma 3 [52]. \square

3.3. Kernel Linearization

Let $G_\sigma(\mathbf{x} - \mathbf{x}') = \exp(-\|\mathbf{x} - \mathbf{x}'\|_2^2 / 2\sigma^2)$ denote a standard Gaussian RBF kernel centered at \mathbf{x}' and having a bandwidth σ . Kernel linearization refers to rewriting this G_σ as an inner-product of two infinite-dimensional feature maps. To obtain these maps, we use a fast approximation method based on probability product kernels [31]. Specifically, we employ the inner product of d'' -dimensional isotropic Gaussians given $\mathbf{x}, \mathbf{x}' \in \mathbb{R}^{d''}$. Thus, we have:

$$G_\sigma(\mathbf{x} - \mathbf{x}') = \left(\frac{2}{\pi\sigma^2} \right)^{\frac{d''}{2}} \int_{\zeta \in \mathbb{R}^{d''}} G_{\sigma/\sqrt{2}}(\mathbf{x} - \zeta) G_{\sigma/\sqrt{2}}(\mathbf{x}' - \zeta) d\zeta. \quad (3)$$

Eq. (3) is then approximated by replacing the integral with the sum over Z pivots ζ_1, \dots, ζ_Z , thus yielding a feature map ϕ as:

$$\phi(\mathbf{x}; \{\zeta_i\}_{i \in \mathcal{I}_Z}) = \left[G_{\sigma/\sqrt{2}}(\mathbf{x} - \zeta_1), \dots, G_{\sigma/\sqrt{2}}(\mathbf{x} - \zeta_Z) \right]^T, \quad (4)$$

$$\text{and } G_\sigma(\mathbf{x} - \mathbf{x}') \approx \langle \sqrt{c}\phi(\mathbf{x}), \sqrt{c}\phi(\mathbf{x}') \rangle, \quad (5)$$

where c is a const. Eq. (5) is the linearization of the RBF kernel. Eq. (4) is the feature map. $\{\zeta_i\}_{i \in \mathcal{I}_Z}$ are pivots. As we use 1 dim. signals, we simply cover interval $[0; 1]$ with Z equally spaced pivots. For clarity, we drop $\{\zeta_i\}_{i \in \mathcal{I}_Z}$ and write $\phi(\mathbf{x})$, *etc.*

4. Approach

Our pipeline is illustrated in Figure 2. It consists of (i) streams already present in DEEP-HAL [75] such as the FV/BoW streams (dashed red), the High Abstraction Features (HAF) stream and the Optical Flow Features (OFF) which are fed into (ii) the Prediction Network abbreviated as PredNet. In this paper we focus on two non-trivial streams, that is the Object Detection Features and Saliency Detection Features (dashed blue) (ODF and SDF for short).

BoW/FV/OFF streams take the I3D intermediate representations generated from the RGB frames and learn to hallucinate BoW/FV and the I3D optical flow representations via the MSE loss between the ground-truth BoW/FV/OFF and the outputs of BoW/FV/OFF streams. The same MSE loss is applied to the ODF and SDF streams. However, the design of compact ground-truth ODF and SDF descriptors is one of our main contributions.

Moreover, the HAF stream processes the I3D representations before they are combined with the hallucinated streams. PredNet fuses the combined BoW/FV/OFF/HAF and our new ODF and SDF to learn actions on videos. Below, we start by describing how we obtain our ODF and SDF descriptors before we describe modules of DEEP-HAL [75] and our modifications. One change is that we learn weights for the weighted mean pooling (*i.e.*, $\sum_i w'_i \psi / \sum_i w'_i$) of each stream to avoid concatenation of streams, thus we prevent overparametrization. Firstly, we start by the statistical motivation regarding higher-order representations we use in ODF and SDF.

4.1. Statistical Motivation

Before we outline our ODF and SDF descriptors, it is paramount to motivate the use of higher-order statistics on which we build. To compare videos, we want to capture a distribution of local features/descriptors *e.g.*, detection scores. The characteristic function $\varphi_{\mathcal{Y}}(\omega) = \mathbb{E}_{\mathcal{Y}}(\exp(i\omega^T \mathbf{v}))$ describes the probability density $f_{\mathcal{Y}}(\mathbf{v})$ of some video features (local features $\mathbf{v} \sim \mathcal{Y}$). This gives us the following Taylor expansion of the characteristic function:

$$\mathbb{E}_{\mathcal{Y}} \left(\sum_{r=0}^{\infty} \frac{i^r}{r!} \langle \mathbf{v}, \omega \rangle^r \right) \approx \frac{1}{N} \sum_{n=0}^N \sum_{r=0}^{\infty} \frac{i^r}{r!} \langle \uparrow \otimes_r \mathbf{v}_n, \uparrow \otimes_r \omega \rangle = (6)$$

$$\frac{1}{N} \sum_{n=0}^N \sum_{r=0}^{\infty} \frac{i^r}{r!} \left\langle \frac{1}{N} \sum_{n=0}^N \uparrow \otimes_r \mathbf{v}_n, \uparrow \otimes_r \omega \right\rangle = \sum_{r=0}^{\infty} \left\langle \mathcal{X}^{(r)}, \frac{i^r}{r!} \uparrow \otimes_r \omega \right\rangle,$$

where i is the imaginary number, and a tensor descriptor $\mathcal{X}^{(r)} = \frac{1}{N} \sum_{n=0}^N \uparrow \otimes_r \mathbf{v}_n$. In principle, with infinite data and infinite moments, one can fully capture $f_{\mathcal{Y}}(\mathbf{v})$. In practice, first-, second- and third-order moments are typically sufficient, however, second- and third-order tensors grow quadratically and cubically w.r.t. the size of \mathbf{v} . Thus, in what follows, we represent second-order moments not by a covariance matrix but by the subspace corresponding to the top n' leading eigenvectors. We also make use of the corresponding eigenvalues of the signal. Finally, it suffices to notice that $\kappa^{(r)} = \text{diag}(\mathcal{X}^{(r)})$ corresponds to the notion of order r cumulants used in calculations of skewness ($r=3$) and kurtosis ($r=4$) but it grows linearly w.r.t. the size of \mathbf{v} . Thus, in what follows, we use the ℓ_2 normalized mean, leading eigenvectors (and trace-normalized eigenvalues), skewness and kurtosis (rather than coskewness and cokurtosis) to obtain compact representation of ODF and SDF.

4.2. Object Detection Features

Each object bounding box is described by the feature vector of the following form:

$$\mathbf{v} = \left[\delta(y_{(det)}); \mathbf{y}_{(inet)}; \phi(\varsigma); \odot_{i \in \mathcal{I}_4} \phi(v_i); \phi\left(\frac{t-1}{\tau-1}\right) \right] \in \mathbb{R}^d, \quad (7)$$

where $\delta = [0, \dots, 1, \dots, 0]^T$ is a vector with all zeros but a single 1 placed at the location y . As we have 91 object classes for detectors trained on the COCO dataset and 80 classes for a detector trained on the AVA v2.1 dataset, we simply assume $y_{(det)} \in \mathcal{I}_{91+80}$, that is, the labels 0, ..., 91 describe classes from COCO while classes 92, ..., 80+91 describe classes from AVA v2.1. Moreover, $\mathbf{y}_{(inet)} \in \mathbb{R}^{1001}$ is an ℓ_1 normalized ImageNet class. score, $0 \leq \varsigma \leq 1$ is the detector confidence score, v_0, \dots, v_4 are the top-left and bottom-right Cartesian coordinates of a bounding box normalized in range $[0; 1]$, and $(t-1)/(\tau-1)$ is the frame index normalized w.r.t. the video sequence length τ . For feature maps $\phi(\cdot)$ defined in Eq. (4), we simply use $Z=7$ pivots and the σ of RBF is set to 0.5. Finally, for all detections per video from a given detector, we first compute the mean $\mu([\mathbf{v}_1, \dots, \mathbf{v}_N]) \in \mathbb{R}^d$ (we write μ) where N is the total number of detections. Then, we form a matrix $\mathcal{Y} \in \mathbb{R}^{d \times N}$:

$$\mathcal{Y} = \frac{1}{J} \left[\frac{1}{K_1} \left[\odot_{i \in \mathcal{I}_{K_1}}^2 (\mathbf{v}_{i1} - \mu) \right], \dots, \frac{1}{K_J} \left[\odot_{i \in \mathcal{I}_{K_J}}^2 (\mathbf{v}_{iJ} - \mu) \right] \right], \quad (8)$$

where K_j denotes a number of detections per frame $j \in \mathcal{I}_J$, from which we extract higher-order statistical moments as described below. Of course, as N is large and its size varies from video to video, hallucinating \mathcal{Y} directly is not feasible (nor it would possess any useful descriptor properties such as invariance to the bounding box order).

Firstly, we obtain $U\lambda V = \text{svd}(\mathcal{Y})$ rather than $U\lambda^2 U^T = \text{eig}(\mathcal{Y}\mathcal{Y}^T)$ as $N \ll d$, where $U = [\mathbf{u}_1, \mathbf{u}_2, \dots]$. Take $\mathcal{X}^{(t)}(\{\mathbf{v} - \mu\}_{n=0}^N)$ (which we abbreviate below simply to $\mathcal{X}^{(t)}$) and $\kappa^{(r)} = \text{diag}(\mathcal{X}^{(r)})$ defined in Section 4.1. Then, we form our multi-moment descriptor $\psi_{(det)} \in \mathbb{R}^{d(4+n')}$:

$$\psi_{(det)} = \left[\frac{\mu}{\|\mu\|_2}; \odot_{i \in \mathcal{I}_{n'}}^2 \mathbf{u}_i(\mathcal{X}^{(2)}); \frac{\kappa^{(3)}}{(\kappa^{(2)})^{3/2}}; \frac{\kappa^{(4)}}{(\kappa^{(2)})^2}; \frac{\text{diag}(\lambda^2)}{\sum_i \lambda_{ii}^2} \right], \quad (9)$$

where $n' \geq 1$. The composition of Eq. (9) is described in Section 4.1. It is easy to verify that $\frac{\kappa^{(3)}}{(\kappa^{(2)})^{3/2}}$ and $\frac{\kappa^{(4)}}{(\kappa^{(2)})^2}$ are the empirical versions of skewness and kurtosis given by $\frac{\mathbb{E}_{\mathcal{Y}}((\mathbf{v} - \mu)^3)}{\mathbb{E}_{\mathcal{Y}}^{3/2}((\mathbf{v} - \mu)^2)}$ and $\frac{\mathbb{E}_{\mathcal{Y}}((\mathbf{v} - \mu)^4)}{\mathbb{E}_{\mathcal{Y}}^2((\mathbf{v} - \mu)^2)}$, respectively.

4.3. Saliency Detection Features

Firstly, we extract directional gradients from saliency frames with discretised gradient operators $[-1, 0, 1]$ and $[-1, 0, 1]^T$. Next, we obtain gradient amplitude and orientation maps Λ and θ per frame which we encode by:

$$\mathbf{v}' = \sum_{i \in \mathcal{I}_W, j \in \mathcal{I}_H} \Lambda_{ij} \phi(\theta_{ij}/(2\pi)) \otimes \phi\left(\frac{i-1}{W-1}\right) \otimes \phi\left(\frac{j-1}{H-1}\right), \quad (10)$$

where \otimes is the Kronecker product and $\phi(\theta)$ follows Eq. (4) with the exception that the assignment to Gaussians is realized in the modulo ring to respect the periodical nature

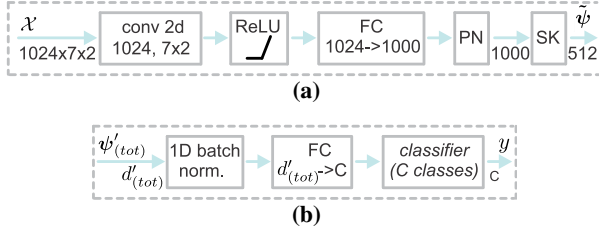


Figure 3: Stream details. Figure 3a shows the stream architecture used by us for the FV, BoW, OFF, HAF, DET1, ..., DET4, SAL1 and SAL2 streams. Figure 3b shows our PredNet. Operation and their parameters are in each block *e.g.*, *conv2d* and its number of filters/size, *Power Normalization* (PN) and *Sketching* (SK). We indicate the size of input and/or output under arrows.

of $0 \leq \theta \leq 2\pi$. We encode $\phi(\theta)$ with 12 pivots which encode the orientation of gradients. The remaining maps $\phi(\cdot)$ are encoded with 5 pivots each, which correspond to spatial binning. One can easily verify that $\mathbf{v}'_{(sal)}$ is similar to a single CKN layer [47] but is simpler in design as for one dimensional variables we sample pivots (*c.f.* learn) for maps $\phi(\cdot)$. Each saliency frame is then described as a feature vector $\mathbf{v}^\dagger = [\mathbf{v}' / \|\mathbf{v}'\|_2; \mathbf{I} / \|\mathbf{I}\|_1] \in \mathbb{R}^{d^\dagger}$, where \mathbf{I} denotes a vectorized low-resolution saliency map. Thus, \mathbf{v}^\dagger represents the directional gradient statistics as well as the intensity-based gist of saliency maps. Subsequently, we compute the mean $\boldsymbol{\mu}([\mathbf{v}_1^\dagger, \dots, \mathbf{v}_J^\dagger]) \in \mathbb{R}^{d^\dagger}$ (we simply write $\boldsymbol{\mu}$) where J is the total number of frames per video. Then, we obtain $\mathcal{R}^\dagger = [\mathbf{v}_1^\dagger, \dots, \mathbf{v}_J^\dagger] / J \in \mathbb{R}^{d^\dagger \times J}$ which is compactly described by the multi-moment Eq. (9) resulting in $\psi_{(sal)} \in \mathbb{R}^{d(4+n^\dagger)}$.

4.4. Hallucinating Streams/High Abstraction Feat.

Each hallucinating stream takes as input the I3D intermediate representation $\mathcal{X}_{(rgb)}$ of size 1024×7 obtained by removing the classifier and the last 1D conv. layer of I3D pre-trained on Kinetics-400. For the BoW/FV/OFF and HAL streams, we follow the steps described in the DEEP-HAL approach [75]. For all streams, we use a Fully Connected (FC) unit shown in Figure 3a. Each stream uses Power Normalization (PN) realized via SigmE and Sketching (SK) from 1000 to 512 dim via $\tilde{\psi}'_{(\cdot)} = \tilde{P}_{(\cdot)} \psi'_{(\cdot)}$. We have introduced sketching into the hallucination stream after PN as this results in a simple linear combination of non-linear decisions due to PN which worked well in practice. The outputs $\tilde{\psi}'$ can be now aligned with ground-truth $\psi'_{(\cdot)}$ described below. The same steps are applied to High Abstraction Features (HAF) which are combined with other streams and also fed into PredNet (see Fig. 2). While hallucinating streams co-supervise I3D via external ground-truth tasks, HAF simply passes I3D features into PredNet.

Ground-truth BoW/FV/OFF. We follow the DEEP-HAL setup [75] and apply PCA to a concatenation of IDT trajectories (30 dim.), HOG (96 dim.), HOF (108 dim.), MBHx (96 dim.) and MBHy (96 dim.). The resulting 213 dim.

local descriptors are encoded by FV and BoW with a 256 dim. and a 1000 dim. GMM and k-means dictionaries, resp. For the OFF stream, we pre-computed I3D with LDOF $\mathcal{X}_{(opt.)}$ (Fig. 2). All ground-truth representations were Power Normalized by SigmE/sketched to 512 dim. each via $\psi'_{(\cdot)} = P_{(\cdot)} \psi_{(\cdot)}$ and fed into the MSE loss. No ground-truth testing data is used at training/testing time.

Ground-truth DET1, ..., DET4/SAL1/SAL2. The ODF ground-truth training representations are of size $1214 \times N$, where N is the total number of bounding boxes per video (approx. from 50 to 10000). The feature dim. 1214 is composed of $80 + 91$ dim. one-hot detection classes, 6×7 are the $\phi(\cdot)$ -embedded confidence, bounding box coordinates and the frame number, 1001 is the ImageNet score. We also consider a variant without the RBF embedding, $\phi(\mathbf{x}) = \mathbf{x}$ of size $1178 \times N$. The SDF ground-truth training representations are of size $556 \times J$, where J is the number of frames per video. 300 dim. ($12 \times 5 \times 5$) concern spatio-angular gradient distributions and 256 dim. (16×16) concern the luminance of saliency maps. Each ODF and SDF is then encoded per video with the multi-moment descriptor in Eq. (9) which yields $1178 \times (4 + n')$ and $556 \times (4 + n^\dagger)$ compact representations (we vary n' and n^\dagger between 1 and 5). Finally, ODF and SDF are Power Normalized by SigmE/sketched to 512 dim. each via $\psi'_{(\cdot)} = P_{(\cdot)} \psi_{(\cdot)}$ and fed into the MSE loss. No ground-truth testing rep. were used for training/testing.

4.5. Objective Function

During training, we combine MSE loss functions which co-supervise hallucination streams with the classifier:

$$\ell^*(\mathcal{X}, \mathbf{y}; \bar{\Theta}) = \frac{\alpha}{|\mathcal{H}|} \sum_{i \in \mathcal{H}} \|\tilde{\psi}_i - \psi'_i\|_2^2 + \ell(f(\psi'_{(tot)}; \Theta_{(pr)}), \mathbf{y}; \Theta_{(\ell)}),$$

where: $\forall i \in \mathcal{H}, \tilde{\psi}'_i = \tilde{P}_i g(\tilde{h}(\mathcal{X}, \Theta_i), \eta)$, $\psi'_i = P_i \psi_i$,

$$\psi'_{(haf)} = P_{(haf)} g(\tilde{h}(\mathcal{X}, \Theta_{(haf)}), \eta),$$

$$\psi'_{(tot)} = \frac{1}{|\mathcal{H}^*| + 1} \left(w_{(haf)} \psi'_{(haf)} + \sum_{i \in \mathcal{H}^*} w_i \tilde{\psi}'_i \right),$$

$$\tilde{\psi}'_{(det)} = \frac{1}{|\mathcal{D}|} \sum_{i \in \mathcal{D}} w_i \tilde{\psi}'_i, \tilde{\psi}'_{(sal)} = \frac{1}{|\mathcal{S}|} \sum_{i \in \mathcal{S}} w_i \tilde{\psi}'_i. \quad (11)$$

The above equation is a trade-off between the MSE loss functions $\{\|\tilde{\psi}'_i - \psi'_i\|_2^2, i \in \mathcal{H}\}$ and the classification loss $\ell(\cdot, \mathbf{y}; \Theta_{(\ell)})$ with some label $\mathbf{y} \in \mathcal{Y}$ and parameters $\Theta_{(\ell)} \equiv \{\mathbf{W}, \mathbf{b}\}$. The trade-off is controlled by $\alpha \geq 0$ while MSE is computed over hall. streams $i \in \mathcal{H}$, and $\mathcal{H} \equiv \{(fv1), (fv2), (bow), (off), (det1), \dots, (det4), (sal1), (sal2)\}$ is our set of hallucination streams. Moreover, $g(\cdot, \eta)$ is a Power Norm. in Eq. (1), $f(\cdot; \Theta_{(pr)})$ is the PredNet module with parameters $\Theta_{(pr)}$ which we learn, $\{\tilde{h}(\cdot, \Theta_i), i \in \mathcal{H}\}$ are the hallucination streams while $\{\tilde{\psi}_i, i \in \mathcal{H}\}$ are the corresponding hallucinated BoW/FV/OFF/ODF/SDF representations. We set $\alpha = 1$.

Moreover, $\tilde{h}(\cdot, \Theta_{(haf)})$ is the HAF stream with the sketched output $\psi'_{(haf)} = P_{(haf)}\psi_{(haf)}$. For the hallucination streams, we learn parameters $\{\Theta_i, i \in \mathcal{H}\}$ while for HAF, we learn $\Theta_{(haf)}$. The full set of parameters we learn is defined as $\bar{\Theta} \equiv (\{\Theta_i, i \in \mathcal{H}\}, \Theta_{(haf)}, \Theta_{(pr)}, \Theta_{(\ell)})$. Furthermore, $\{\tilde{P}_i, i \in \mathcal{H}\}$ and $\{P_i, i \in \mathcal{H}\}$ are the projection matrices for count sketching of streams $\{\tilde{\psi}_i, i \in \mathcal{H}\}$ and the ground-truth feature vectors $\{\psi_i, i \in \mathcal{H}\}$. Finally, for $\psi'_{(tot)}$ is a weighted average of several streams fed into the PredNet module f . Moreover, $\mathcal{H}^* \equiv \{(fv1), (fv2), (bow), (off), (det), (sal)\}$, $\mathcal{D} \equiv \{(det1), \dots, (det4)\}$ and $\mathcal{S} \equiv \{(sal1), (sal2)\}$. Section 3.2 details how to select matrices P . Let \mathcal{T} be set to either \mathcal{H}^* , \mathcal{D} or \mathcal{S} , then our weights are:

$$w_i = \frac{1}{|\mathcal{T}|} \frac{\max(w_i^\beta, \rho)}{\sum_{j \in \mathcal{T}} \max(w_j^\beta, \rho)}, \quad (12)$$

Prior to CNN training, we train an SVM on each ground-truth stream separately (using a manageable training subset), and we set weights w' proportionally to the accuracies obtained on the validation set. For the HAF stream, we simply set $w'_{(haf)} = \frac{1}{|\mathcal{H}^*|+1}$ and $\rho = 0.1$. For the first few epochs (i.e., 10), we set $\beta = 0$ so that all streams receive equal weights. Subsequently, in each epoch, we run the Golden-section search to find the best $\beta \geq 0$. We start from initial boundary values $\beta \in \{0, 50\}$, we train an SVM on a manageable subset of training data and evaluate on the validation set β as it gets closer to maximizing the accuracy, and we update boundary values for the next epoch accordingly. Eq. (12) has a nice property: for $\beta = 0$, we have $w_i = 1/|\mathcal{T}|$. For $\beta \rightarrow \infty$, we have $w_i = 1$ if $w_i = \max(\{w_i\}_{i \in \mathcal{T}})$, otherwise $w_i = 0$. Thus, β interpolates between equalizing all weights and the winner-takes-all solution.

5. Experiments

5.1. Datasets and Evaluation Protocols

HMDB-51 [42] consists of 6766 internet videos over 51 classes; each video has ~ 20 –1000 frames. We report the mean accuracy across three splits.

YUP++ [19] contains 20 scene classes of so-called video textures, 60 videos per class, and the splits contain scenes captured by either the static or moving camera. We use the standard splits (1/9 dataset for training) for evaluation.

MPII Cooking Activities [57] contains high-resolution videos of people cooking dishes. The 64 activities from 3748 clips include coarse actions e.g., *opening refrigerator*, and fine-grained actions e.g., *peel*, *slice*, *cut apart*. We use the mean Average Precision (mAP) over 7-fold cross validation. For human-centric protocol [6, 8], we use the faster RCNN [55] to crop video around human subjects.

Charades [61] consist of 9848 videos of daily indoors activities, 66500 clip annotations and 157 classes.

	<i>sp1</i>	<i>sp2</i>	<i>sp3</i>	mean acc.
<i>det1</i>	42.00%	39.74%	40.39%	40.72%
<i>det1</i>	40.49%	40.13%	39.67%	40.09%
<i>det3</i>	43.78%	44.05%	41.97%	43.26%
<i>det4</i>	41.08%	39.22%	40.39%	40.23%
<i>all+avg</i>	42.50%	41.05%	41.01%	41.52%
<i>all+max</i>	43.25%	42.32%	42.09%	42.55%
<i>all+wei</i>	45.80%	44.52%	44.09%	44.80%
<i>DEEP-HAL+all+avg</i>	83.25%	82.24%	82.84%	82.77%
<i>DEEP-HAL+all+max</i>	83.18%	81.86%	82.84%	82.62%
<i>DEEP-HAL+all+wei</i>	84.01%	83.25%	83.10%	83.45%

Table 1: Evaluations of ODF on HMDB-51. (*top*) We evaluate backbones such as (*det1*) Inception V2, (*det2*) Inception ResNet V2, (*det3*) ResNet101 and (*det4*) NASNet. (*middle*) The average-pooled, max-pooled and the weighted mean combination of all detectors are given by (*all+avg*), (*all+max*) and (*all+wei*). (*bottom*) Pre-trained DEEP-HAL combined with all four detectors by the average-pooling, max-pooling and the weighted mean.

	<i>avg</i>	<i>max</i>	<i>wei</i>
<i>all</i>	55.12%	42.34%	60.52%
<i>DEEP-HAL+all</i>	74.22%	71.85%	75.74%

Table 2: Pooling on YUP++. Results for the average-pooled (*avg*), max-pooled (*max*) and the weighted mean (*wei*) of all detectors (*all*) vs. pre-trained DEEP-HAL combined with all detectors by the average-pooling, max-pooling and the weighted mean.

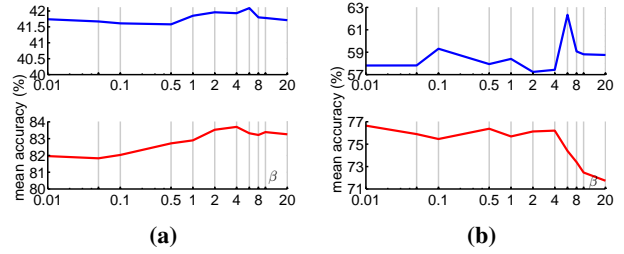


Figure 4: The impact of β in the weighted mean on the classification results. Figure 4a shows results for HMDB-51 on (*top*) four detectors combined+SVN and (*bottom*) DEEP-HAL with four detectors combined+SVN. Figure 4b shows results for YUP++.

5.2. Evaluations

Below, we show the effectiveness of our approach. Firstly, we evaluate various components of our design.

Ground-truth ODF+SVN. Firstly, we evaluate our ODF on SVN given the HMDB-51 dataset. We set $n' = 3$ for Eq. (9) and compare various detector backbones and pooling strategies. Table 1 shows that all detectors perform similarly with (*det3*) being slightly better than other methods. Moreover, max-pooling on ODFs from all four detectors is marginally better than the average-pooling. However, only the weighted mean (*all+wei*) according to Eq. (12) appears to outperform (*det3*) which highlights the need for the robust aggregation of ODFs. Similarly, when we combine pre-trained DEEP-HAL with all detectors, the weighted mean (*DEEP-HAL+all+wei*) performs best. Table 2 shows the similar trend on YUP++ for which the weighted mean

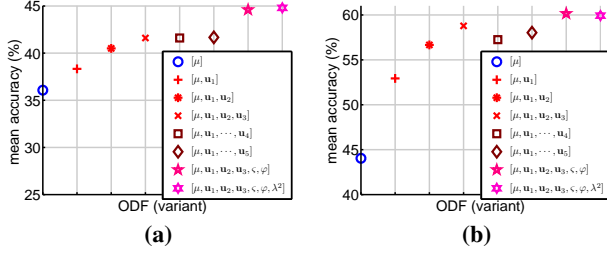


Figure 5: ODF eval. on SVM on four detectors (the weighted mean). Fig. 5a and 5b show results on HMDB-51 and YUP++. μ , $\mathbf{u}_1, \dots, \mathbf{u}_i, \varsigma, \varphi$, and λ^2 correspond to the entries in Eq. (9).

(*all+wei*) outperforms the average-pooling by $\sim 4\%$. We trained SVM only on videos for which at least one successful detection occurred, thus a 75.74% accuracy is much lower than the main results reported on the full pipeline which copes with missing detections by skipping a stream update if a ground-truth descr. is missing. Figure 4 shows that parameter $\beta \neq 1$ has a positive impact on reweighting.

Ground-truth SDF. The SDF on HMDB-51 and YUP++ yielded 24.35% and 32.68% accuracy. This is expected as SDFs do not capture a discriminative information per se but they locate salient spatial and temporal regions to co-supervise and point the main network to important regions.

Multi-moment descr. Figure 5 shows that the concat. of the mean and three eigenvectors according to Eq. (9) yields good results but adding further vectors deteriorates the performance. However, adding skewness and kurtosis (ς and φ) further improves results, while adding eigenvalues has a limited impact. Thus, overrepresentation of the probability density with the full covariance (or too many eigenvectors) best be avoided in favor of using higher-order moments.

HMDB-51. Table 3 shows several DEEP-HAL variants, which all hallucinate BoW/FV/OFF. DEEP-HAL with our reweighting mechanism (*DEEP-HAL+W*) outperforms the original DEEP-HAL denoted as (*HAF/BoW/FV hal.*) [75] by $\sim 0.8\%$. DEEP-HAL with our ODF and SDF descriptors (*DEEP-HAL+ODF*) and (*DEEP-HAL+SDF*) outperform (*HAF/BoW/FV hal.*) by $\sim 1.8\%$ and $\sim 1.4\%$, resp. This shows that both ODF and SDF are effective, thus co-supervising AR pipelines with object and saliency hypotheses appears a valid training strategy. Combining DEEP-HAL, ODF and SDF outperform DEEP-HAL by $\sim 2.7\%$ demonstrating the complementary nature of ODF and SDF. Utilizing our weighting mechanism with DEEP-HAL, ODF and SDF denoted as (*DEEP-HAL+W+ODF+SDF*) outperform (*HAF/BoW/FV hal.*) by $\sim 4.6\%$. Finally, DEEP-HAL with weighting, and ODF and SDF with RBF feature maps from Eq. (4) outperform (*HAF/BoW/FV hal.*) by $\sim 5.1\%$.

YUP++. Table 4 shows that ODF is better than SDF, that is (*DEEP-HAL+ODF*) and (*DEEP-HAL+SDF*) outperform (*HAF/BoW/FV hal.*) by $\sim 0.6\%$ and $\sim 0.2\%$, resp. This is expected as YUP++ contains dynamic

	<i>sp1</i>	<i>sp2</i>	<i>sp3</i>	mean acc.
<i>DEEP-HAL+W</i>	83.94%	82.50%	83.34%	83.26%
<i>DEEP-HAL+ODF</i>	85.03%	83.59%	84.25%	84.29%
<i>DEEP-HAL+SDF</i>	84.64%	83.20%	83.82%	83.88%
<i>DEEP-HAL+ODF+SDF</i>	86.14%	83.66%	85.81%	85.20%
<i>DEEP-HAL+W+ODF+SDF</i>	87.78%	86.27%	87.06%	87.04%
<i>DEEP-HAL+W+G+ODF+SDF</i>	88.37%	86.80%	87.52%	87.56%
ADL+I3D 81.5% [74]	Full-FT I3D 81.3% [4]			
EvaNet (Ensemble) 82.3% [53]	PA3D + I3D 82.1% [80]			
HAF/BoW/FV exact 82.50% [75]	HAF/BoW/FV hal. 82.48% [75]			

Table 3: Evaluations of (*top*) our methods and (*bottom*) comparisons to the state of the art on HMDB-51.

	<i>static</i>	<i>dynamic</i>	<i>mixed</i>	mean stat/dyn	mean all
<i>DEEP-HAL+ODF</i>	95.00%	90.93%	93.52%	93.0%	93.2%
<i>DEEP-HAL+SDF</i>	94.96%	89.93%	93.58%	92.4%	92.8%
<i>DEEP-HAL+SDF+ODF</i>	95.10%	91.11%	93.61%	93.1%	93.3%
<i>DEEP-HAL+W+SDF+ODF</i>	96.30%	92.22%	94.17%	94.3%	94.2%
<i>DEEP-HAL+W+G+SDF+ODF</i>	96.30%	92.40%	94.35%	94.4%	94.4%
T-ResNet [19]	92.4%	81.5%	89.0%	87.0%	87.6%
ADL I3D [74]	95.1%	88.3%	-	91.7%	-
HAF/BoW/FV hal. [75]	94.8%	89.6%	93.3%	92.2%	92.6%
MSOE-two-stream [26]	97.0%	87.0%	91.8%	92.0%	91.9%

Table 4: Evaluations of (*top*) our methods and (*bottom*) comparisons to the state of the art on YUP++.

	<i>sp1</i>	<i>sp2</i>	<i>sp3</i>	<i>sp4</i>	<i>sp5</i>	<i>sp6</i>	<i>sp7</i>	mAP
<i>DEEP-HAL+W+ODF+SDF</i>	82.5	85.1	85.6	83.5	86.6	80.8	81.2	83.6%
<i>DEEP-HAL+W+G+ODF+SDF</i>	83.3	87.6	85.6	83.4	86.6	83.2	83.6	84.8%
KRP-FS+IDT 76.1% [8]	GRP+IDT 75.5% [6]							
I3D+BoW/OFF MTL 79.1% [75]	HAF/BoW/OFF hal. 81.8% [75]							

Table 5: Evaluations of (*top*) our methods and (*bottom*) comparisons to the state of the art on MPII.

HAF/BoW/FV hal. [75]	<i>DEEP-HAL+W+G+ODF (SK512)</i>	<i>DEEP-HAL+W+G+SDF (SK512)</i>
43.1	47.22	45.30
<i>DEEP-HAL+W+G+ODF+SDF (SK512)</i>	<i>DEEP-HAL+W+G+ODF+SDF (SK1024)</i>	<i>DEEP-HAL+W+G+ODF+SDF (exact)</i>
49.06	50.14	50.16

Table 6: Evaluations of our methods on the Charades dataset.

scenes without objects/specific saliency regions correlating with class concepts. However, a combination of detectors/saliency (*DEEP-HAL+SDF*) plus weighting (*DEEP-HAL+W+ODF+SDF*) plus the RBF maps (*DEEP-HAL+W+G+ODF+SDF*) outperform (*HAF/BoW/FV hal.*) by $\sim 0.7\%$, $\sim 1.6\%$ and $\sim 1.8\%$ accuracy, resp.

MPII. Table 5 shows that we obtain $\sim 3.0\%$ mAP improvement over (*HAF/BoW/FV hal.*) due to detectors capturing the human interaction with objects.

Charades. Table 6 (top) presents relative gains of our hallucination pipeline (*DEEP-HAL*) with weighted mean pooling (*W*) and the RBF maps (*G*) denoted as (*DEEP-HAL+W+G*).

	<i>sp1</i>	<i>sp2</i>	<i>sp3</i>	mean acc.
<i>wei+flat</i>	86.47%	85.56%	86.27%	86.10%
<i>wei+3 levels</i>	88.37%	86.80%	87.52%	87.56%

Table 7: Evaluations of the flat single level weighted mean (*wei+flat*) vs. three levels of weighted mean pooling (*wei+3 levels*) on HMDB-51.

We evaluate Object Detection Features (*ODF*) and Saliency Detection Features (*SDF*) after applying 512 dim. sketching (*SK512*). See our main paper for the details of the sketch operation. The table shows that (*DEEP-HAL+W+G+ODF (SK512)*) outperforms (*DEEP-HAL+W+G+SDF (SK512)*), and both methods outperform the baseline (*HAF/BoW/FV hal.*) [75] which highlights the usefulness of the *ODF* and *SDF* descriptors.

Table 6 (bottom) shows that combining *ODF* and *SDF* into (*DEEP-HAL+W+G+SDF+ODF (SK512)*) yields 49.06% mAP which constitutes on a $\sim 6\%$ gain over the baseline (*HAF/BoW/FV hal.*) [75]. This demonstrates that *ODF* and *SDF* are highly complementary. Furthermore, applying a larger sketch (*DEEP-HAL+W+G+ODF+SDF (SK1024)*) yields 50.14% mAP which matches the use (*DEEP-HAL+W+G+ODF+SDF (exact)*) that denotes a late fusion by concatenation of *ODF* and *SDF* with the stream resulting from *DEEP-HAL* fed into *PredNet*. Note that (*exact*) indicates that *ODF* and *SDF* are not hallucinated at the test time but they are computed on the testing data. Thus, the results matching between (*DEEP-HAL+W+G+ODF+SDF (SK1024)*) and (*DEEP-HAL+W+G+ODF+SDF (exact)*) demonstrate that we can hallucinate *ODF* and *SDF* at the test time while regaining the full performance. This is especially important as the main proposal of our idea is to save computational time and hallucinate the detection and saliency features which boost the results on Charades by $\sim 6\%$ compared to the baseline on which we build.

In contrast, the best currently reported papers such as *SlowFast* networks [17] and *AssembleNet* [59] achieve 45.2% and 51.6% on Charades. We note the latter paper is not peer-reviewed yet (as far as we can tell). We further note that *SlowFast* networks and *AssembleNet* backbones can be used in place of *I3D* in our experimental setup, thus our approach is ‘orthogonal’ to these latest developments which focus on heavy mining for combinations of neural blocks/dataflow between them to obtain an ‘optimal’ pipeline. We achieve similar results with a much more principled approach based on multi-task and transfer learning which makes our pipeline lightweight in comparison to competitors as we have no need for computations of the optical flow, or detections and saliency on the test data at all.

Global ImageNet vs. object detectors. Various scores from the object and saliency detectors which we use cannot

	<i>no. of frames</i>	<i>av. frame count</i>	<i>no. of videos</i>	<i>no. of clips</i>	<i>no. of classes</i>
HMDB-51	628635	92.91	6766	6766	51
YUP++	166463	138.72	1200	1200	20
MPII	662394	176.73	44	3748	60
Charades	19978821	300.51	9848	66500	157

Table 8: Statistics of datasets used in our experimnts.

be plugged directly into the *DEEP-HAL* due to the varying number of objects detected and the varying number of frames, thus we propose and use *ODF* and *SDF* descriptors. We also note that using a simplified variant of *ODF* which stacks up ImageNet scores per frame into a matrix (no detectors) to which we apply our multi-moment descriptor yielded $\sim 4\%$ worse results than our *DEEP-HAL+ODF* (detectors-based approach) which yields 48.0% mAP. This is expected as ImageNet is trained in a multi-class setting (one object per image) while detectors let us model robustly distributions of object classes and locations per frame.

6. Reweighting mechanism

In this experiment, we employ pipeline (*DEEP-HAL+W+G+SDF+ODF (SK512)*) explained above. Typically, we use three levels of weighting mean pooling which are applied to (i) four object detectors constituting on *ODF*, (ii) two saliency detectors constituting on *SDF*, and (iii) the final combination of *HAF/BoW/FV/OFF/ODF/SDF*. Thus, below we investigate the performance of a single weighting mean pooling step applied simultaneously to four object detectors, two saliency detectors and the remaining streams.

Table 7 shows that using a flat single level weighted mean pooling yields 86.1% accuracy on the HMDB-51 which is a $\sim 1.4\%$ less compared to utilizing three levels of weighted mean pooling. We expect that having one weighted mean pooling per modality is a reasonable strategy as for instance object category detectors may yield similar responses thus they should be first reweighted for the best ‘combined detector’ performance before being combined with highly complementary modalities.

Finally, Figure 8 (top) demonstrates how our Golden-search selects optimal β on the validation set of MPII (*split1*). Figure 8 (bottom) demonstrates the corresponding validation mAP (this is not the mAP score on the testing set). Note that for the first 10 epochs we use $\beta = 0$ and we start the Golden-search from epoch 11.

7. Dataset statistics and timing

Table 8 shows basic statistics re. datasets used in our experiments. We note that Charades with 66500 uniquely annotated clips, 157 action labels and an average frame count of 300 per clip is the largest among these datasets.

Table 9 introduces timing for object detectors used by our *ODF* descriptors during training. We note that detections with all four object detectors which we use take ~ 1.47

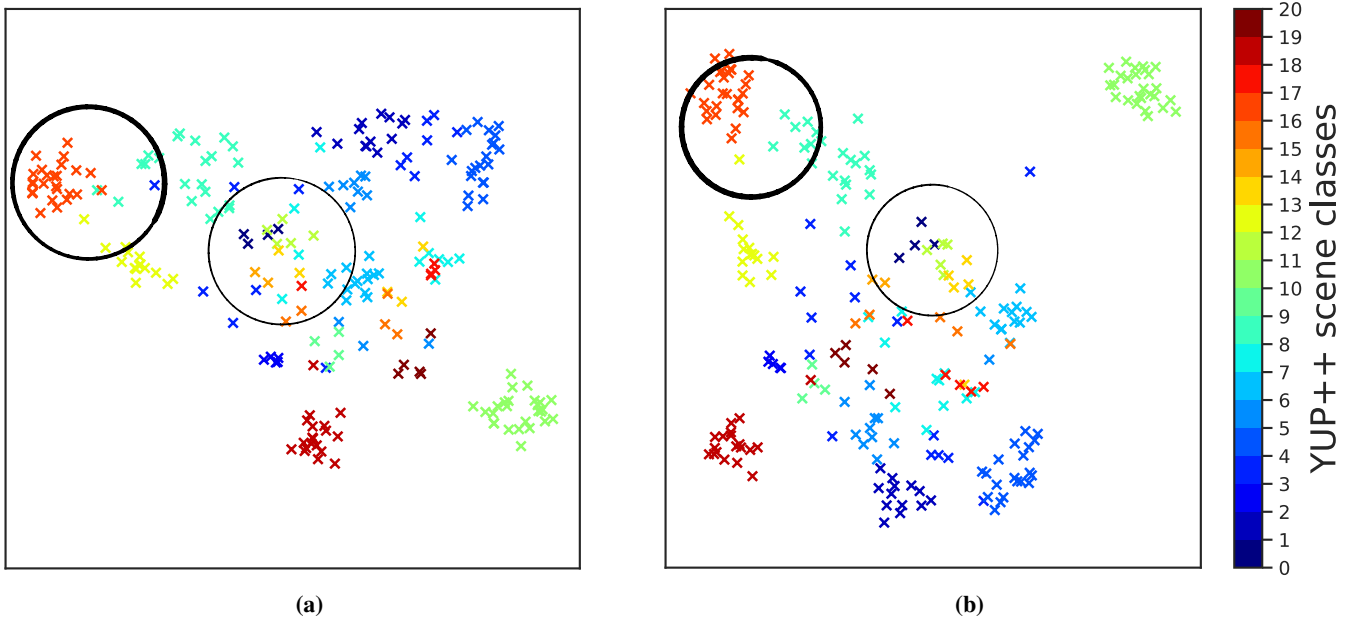


Figure 6: Visualization of the feature space (from PredNet) for DEEP-HAL in Fig. 6a and DEEP-HAL+ODF in Fig. 6b on the YUP++ dataset. For comparison, we circle regions with interesting changes.

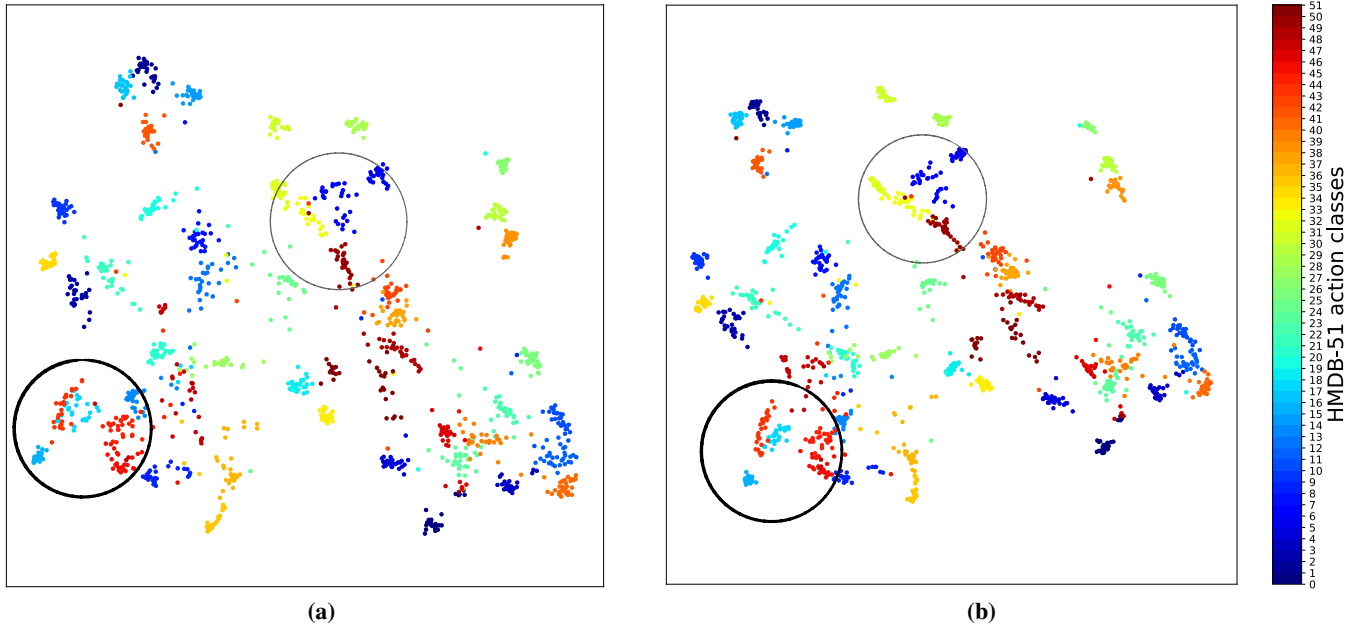


Figure 7: Visualization of the feature space (from PredNet) for DEEP-HAL in Fig. 7a and DEEP-HAL+ODF in Fig. 7b on the HMDB-51 dataset. For comparison, we circle regions with interesting changes.

second per frame. Thus, obtaining four ODF descriptors per clip (uniquely annotated sequence to train or classify) takes between 136 and 441 seconds. Table 10 introduces timing for saliency detectors used in our SDF descriptors during training. We note that detections with both saliency detectors which we use take ~ 0.9 second per frame, and obtaining both SDF descriptors per clip takes between 84 and

271 seconds. We do note that the major computational cost is incurred due to detectors rather than our ODF and SDF descriptors proposed in the main paper (their cost is minimal). We further note that the idea of learning these costly representations during training is very valuable. While the total computations per training clip vary between 220 and 712 seconds, during testing time we obtain these represen-

	DET1: Inception V2	DET2: Inception ResNet V2	DET3: ResNet101 AVA	DET4: NASNet	ODF total (+SVD)
<i>sec. per frame</i>	0.07	0.38	0.10	0.91	1.46 (+0.09)
<i>s.p.c.</i> HMDB-51	6.5	35.3	9.3	84.5	135.6 (+0.5)
<i>s.p.c.</i> YUP++	9.7	52.7	13.9	126.2	202.5 (+0.8)
<i>s.p.c.</i> MPII	12.4	67.1	17.7	160.8	258.0 (+1.3)
<i>s.p.c.</i> Charades	21.0	114.2	30.0	273.5	438.7 (+2.6)

Table 9: Statistics of object detectors we use. We provide timings such as seconds per frame (*sec. per frame*) and seconds per clip (*s.p.c.*) for detectors used by ODF. The total time incurred by a combined detector (*ODF total*) is also provided. We also compute the time taken by the full SVD and all remaining ODF operations described in the main paper, assuming ~ 5 detections per frame.

	SALI: MNL	SALI: ACLNNet	SDF total (+Eq. (10))	ODF+SDF total (+Eq. (10))+SVD)
<i>sec. per frame</i>	0.60	0.30	0.90 (+0.003)	2.36 (+0.1)
<i>s.p.c.</i> HMDB-51	55.7	27.9	83.6 (+0.3)	219.2 (+0.8)
<i>s.p.c.</i> YUP++	83.2	41.6	124.8 (+0.4)	327.3 (+1.2)
<i>s.p.c.</i> MPII	106.0	53.0	159.0 (+0.5)	417.0 (+1.8)
<i>s.p.c.</i> Charades	180.3	90.1	270.4 (+0.9)	709.1 (+3.5)

Table 10: Statistics of saliency detectors we use. We provide timings such as seconds per frame (*sec. per frame*) and seconds per clip (*s.p.c.*) for detectors used by SDF. The total time incurred by a combined detector (*SDF total*) is also provided. We also compute the time taken by the descriptor in Eq. (10) and all remaining SDF operations described in the main paper. Finally, we also provide the combined ODF and SDF time (*SDF+ODF total*).

tations for free (milliseconds) thanks to DET1,...,DET4 and SAL1/SAL2 units from Figure 2 (the main submission). Assuming 25% of clips in charades for testing, that results in 137 days of computational savings on a single GPU (conversely, 1 day savings on 137 GPUs). Given the obtained 6% boost on Charades over the baseline without ODF and SDF, and the computational savings, we believe these statistics highlight the value of our approach.

8. Visualization using UMAP [48]

Figure 6 is a visualization performed with UMAP [48] on the YUP++ dataset. In Fig. 6a, top left corner contains samples from classes in red, green, and blue colors which partially overlap. In Fig. 6b, top left corner contains the samples from the corresponding classes in red, green, and blue colors. This time, the samples of these three classes are well separated from each other.

Figure 7 is a visualization performed with UMAP [48] on the HMDB-51 dataset. In Fig. 7a, bottom left corner contains samples from classes in red and blue colors which partially overlap. In Fig. 7b, bottom left corner contains the samples from the corresponding classes in red and blue colors. This time, the class-wise clusters seem to be more clearly delineated and samples of these classes are separated better from each other.

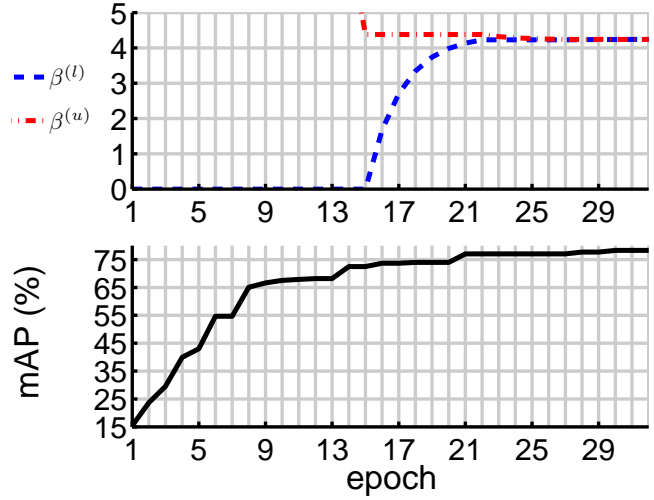


Figure 8: Visualization of the Golden-search for the weighting mechanism (final level weighting). (top) Illustration of how the lower and upper estimates $\beta^{(l)}$ and $\beta^{(u)}$ converge as epochs progress. (bottom) For every epoch, we set $\beta = 0.5(\beta^{(l)} + \beta^{(u)})$ and obtain the corresponding validation score (mAP) on MPII (*split1*). As the epoch number advances, mAP improves and remains stable as the Golden-search algorithm converges.

9. Conclusions

We have introduced two simple yet effective object and saliency descriptors for the use with AR hallucination-based networks. We have shown that modeling high-order statistical moments can result in small representations that can co-supervise our AR pipeline. The findings are in line with recent multi-task learning papers that argue that related tasks can co-regularize the main task. We are the first to hallucinate object and saliency detection cues with clear cut improvements in accuracy.

References

- [1] A. Borji, M. Cheng, H. Jiang, and J. Li. Salient object detection: A benchmark. *TIP*, 24(12):5706–5722, 2015. 3
- [2] Jim Braux-Zin, Romain Dupont, and Adrien Bartoli. A general dense image matching framework combining direct and feature-based costs. In *ICCV*, pages 185–192, 2013. 3
- [3] Thomas Brox and Jitendra Malik. Large displacement optical flow: Descriptor matching in variational motion estimation. *TPAMI*, 33(3):500–513, Mar. 2011. 3
- [4] João Carreira and Andrew Zisserman. Quo Vadis, Action Recognition? A New Model and the Kinetics Dataset. *CVPR*, pages 1–10, 2018. 1, 3, 8
- [5] Bhaskar Chakraborty, Michael B. Holte, Thomas B. Moeslund, and Jordi González. Selective spatio-temporal interest points. *CVIU*, 116(3):396–410, 2012. 3
- [6] Anoop Cherian, Basura Fernando, Mehrta Harandi, and Stephen Gould. Generalized rank pooling for action recognition. In *CVPR*, 2017. 7, 8
- [7] Anoop Cherian, Piotr Koniusz, and Stephen Gould. Higher-

- order pooling of CNN features via kernel linearization for action recognition. In *WACV*, pages 130–138, 2017. 1, 2, 3
- [8] Anoop Cherian, Suvrit Sra, Stephen Gould, and Richard Hartley. Non-linear temporal subspace representations for activity recognition. In *CVPR*, pages 2197–2206, 2018. 1, 2, 3, 7, 8
- [9] Vasileios Choutas, Philippe Weinzaepfel, Jérôme Revaud, and Cordelia Schmid. PoTion: Pose motion representation for action recognition. In *CVPR*, pages 7024–7033, 2018. 1, 2, 3
- [10] Graham Cormode and Marios Hadjieleftheriou. Finding frequent items in data streams. *Proc. VLDB Endow.*, 1(2):1530–1541, Aug. 2008. 4
- [11] Gabriella Csurka, Christopher R. Dance, Lixin Fan, Jutta Willamowski, and Cédric Bray. Visual categorization with bags of keypoints. *ECCV Workshop*, pages 1–22, 2004. 1, 3
- [12] N. Dalal and B. Triggs. Histograms of oriented gradients for human detection. *CVPR*, 1:886–893, 2005. 3
- [13] Navneet Dalal, Bill Triggs, and Cordelia Schmid. Human Detection Using Oriented Histogram of Flow and Appearance. *ECCV*, pages 428–441, 2006. 1, 3
- [14] Piotr Dollár, Vincent Rabaud, Garrison Cottrell, and Serge Belongie. Behavior recognition via sparse spatio-temporal features. In *Proceedings of the 14th International Conference on Computer Communications and Networks*, pages 65–72, 2005. 3
- [15] Jeff Donahue, Lisa Anne Hendricks, Sergio Guadarrama, Marcus Rohrbach, Subhashini Venugopalan, Trevor Darrell, and Kate Saenko. Long-term recurrent convolutional networks for visual recognition and description. In *CVPR*, pages 2625–2634, 2015. 3
- [16] Pengfei Fang, Jieming Zhou, Soumava Kumar Roy, Lars Petersson, and Mehrtash Harandi. Bilinear attention networks for person retrieval. In *ICCV*, 2019. 3
- [17] Christoph Feichtenhofer, Haoqi Fan, Jitendra Malik, and Kaiming He. Slowfast networks for video recognition. In *ICCV*, 2019. 9
- [18] Christoph Feichtenhofer, Axel Pinz, and Richard P. Wildes. Spatiotemporal residual networks for video action recognition. In *NIPS*, pages 3468–3476, 2016. 1, 3
- [19] Christoph Feichtenhofer, Axel Pinz, and Richard P. Wildes. Temporal residual networks for dynamic scene recognition. In *CVPR*, 2017. 7, 8
- [20] Basura Fernando, Efstratios Gavves, José Oramas M., Amir Ghodrati, and Tinne Tuytelaars. Modeling video evolution for action recognition. In *CVPR*, pages 5378–5387, 2015. 3
- [21] Basura Fernando and Stephen Gould. Learning end-to-end video classification with rank-pooling. In *ICML*, volume 48, pages 1187–1196, 2016. 1, 2, 3
- [22] William T. Freeman and Michal Roth. Orientation histograms for hand gesture recognition. Technical Report TR94-03, MERL - Mitsubishi Electric Research Laboratories, Cambridge, MA 02139, Dec. 1994. 3
- [23] Ross Girshick. Fast r-cnn. In *ICCV*, ICCV ’15, pages 1440–1448, 2015. 3
- [24] Ross Girshick, Jeff Donahue, Trevor Darrell, and Jitendra Malik. Region-based convolutional networks for accurate object detection and segmentation. *TPAMI*, 38(1):142–158, Jan. 2016. 3
- [25] Chunhui Gu, Chen Sun, David A. Ross, Carl Vondrick, Caroline Pantofaru, Yeqing Li, Sudheendra Vijayanarasimhan, George Toderici, Susanna Ricco, Rahul Sukthankar, Cordelia Schmid, and Jitendra Malik. Ava: A video dataset of spatio-temporally localized atomic visual actions. In *The IEEE Conference on Computer Vision and Pattern Recognition (CVPR)*, June 2018. 2, 3
- [26] Isma Hadji and Richard P. Wildes. A new large scale dynamic texture dataset with application to ConvNet understanding. In *The European Conference on Computer Vision (ECCV)*, September 2018. 8
- [27] Kaiming He, Georgia Gkioxari, Piotr Dollár, and Ross B. Girshick. Mask r-cnn. *ICCV*, pages 2980–2988, 2017. 3
- [28] Kaiming He, Xiangyu Zhang, Shaoqing Ren, and Jian Sun. Deep residual learning for image recognition. In *The IEEE Conference on Computer Vision and Pattern Recognition (CVPR)*, June 2016. 2, 3
- [29] Berthold K. P. Horn and Brian G. Schunck. Determining optical flow. *Artificial Intelligence*, 17:185–203, 1981. 3
- [30] Qibin Hou, Ming-Ming Cheng, Xiaowei Hu, Ali Borji, Zhuowen Tu, and Philip H. S. Torr. Deeply supervised salient object detection with short connections. In *CVPR*, pages 3203–3212, July 2017. 3
- [31] Tony Jebara, Risi Kondor, and Andrew Howard. Probability product kernels. *JMLR*, 5:819–844, 2004. 4
- [32] Hervé Jégou, Matthijs Douze, and Cordelia Schmid. On the Burstiness of Visual Elements. *CVPR*, pages 1169–1176, 2009. 3
- [33] Shuiwang Ji, Wei Xu, Ming Yang, and Kai Yu. 3D convolutional neural networks for human action recognition. *TPAMI*, 35:221–231, 2010. 3
- [34] Andrej Karpathy, George Toderici, Sanketh Shetty, Thomas Leung, Rahul Sukthankar, and Li Fei-Fei. Large-scale video classification with convolutional neural networks. In *CVPR*, pages 1725–1732, 2014. 3
- [35] Alexander Kläser, Marcin Marszałek, and Cordelia Schmid. A Spatio-Temporal Descriptor Based on 3D-Gradients. *BMCV*, pages 1–10, 2008. 1, 3
- [36] Piotr Koniusz, Anoop Cherian, and Fatih Porikli. Tensor representations via kernel linearization for action recognition from 3D skeletons. *ECCV*, 2016. 3
- [37] Piotr Koniusz and Krystian Mikolajczyk. Soft Assignment of Visual Words as Linear Coordinate Coding and Optimisation of its Reconstruction Error. *ICIP*, 2011. 3
- [38] Piotr Koniusz, Fei Yan, Philippe-Henri Gosselin, and Krystian Mikolajczyk. Higher-order Occurrence Pooling on Mid- and Low-level Features: Visual Concept Detection. *Technical Report*, 2013. 3
- [39] Piotr Koniusz, Fei Yan, Philippe-Henri Gosselin, and Krystian Mikolajczyk. Higher-order occurrence pooling for bags-of-words: Visual concept detection. *TPAMI*, 39(2):313–326, 2017. 3, 4
- [40] Piotr Koniusz, Fei Yan, and Krystian Mikolajczyk. Comparison of Mid-Level Feature Coding Approaches And Pooling Strategies in Visual Concept Detection. *CVIU*, 2012. 3, 4
- [41] Piotr Koniusz, Hongguang Zhang, and Fatih Porikli. A deeper look at power normalizations. In *CVPR*, pages 5774–5783, 2018. 3, 4
- [42] Hildegard Kuehne, Hueihan Jhuang, Estíbaliz Garrote, Tomaso Poggio, and Thomas Serre. HMDB: A large video

- database for human motion recognition. In *ICCV*, pages 2556–2563, 2011. 7
- [43] Ivan Laptev. On space-time interest points. *IJCV*, 64(2-3):107–123, Sept. 2005. 3
- [44] Chuanzhen Li, Bailiang Su, Jingling Wang, and Qin Zhang. Human action recognition using multi-velocity STIPs and motion energy orientation histogram. *J. Inf. Sci. Eng.*, 30:295–312, 2014. 3
- [45] Tsung-Yi Lin, Michael Maire, Serge Belongie, James Hays, Pietro Perona, Deva Ramanan, Piotr Dollár, and C. Lawrence Zitnick. Microsoft coco: Common objects in context. In David Fleet, Tomas Pajdla, Bernt Schiele, and Tinne Tuytelaars, editors, *Computer Vision – ECCV 2014*, pages 740–755. Cham, 2014. Springer International Publishing. 2, 3
- [46] Liu Lingqiao, Lei Wang, and Xinwang Liu. In Defence of Soft-assignment Coding. *ICCV*, 2011. 3
- [47] Julien Mairal, Piotr Koniusz, Zaid Harchaoui, and Cordelia Schmid. Convolutional kernel networks. *NIPS*, 2014. 6
- [48] Leland McInnes, John Healy, Nathaniel Saul, and Lukas Grossberger. Umap: Uniform manifold approximation and projection. *The Journal of Open Source Software*, 3(29):861, 2018. 11
- [49] Nils Papenberg, Andrés Bruhn, Thomas Brox, Stephan Didas, and Joachim Weickert. Highly accurate optic flow computation with theoretically justified warping. *IJCV*, 67:141–158, 2006. 3
- [50] Florent Perronnin and Christopher Dance. Fisher kernels on visual vocabularies for image categorization. *CVPR*, 0:1–8, 2007. 1, 3
- [51] Florent Perronnin, Jorge Sánchez, and Thomas Mensink. Improving the Fisher Kernel for Large-Scale Image Classification. *ECCV*, pages 143–156, 2010. 1, 3
- [52] Ninh Pham and Rasmus Pagh. Fast and scalable polynomial kernels via explicit feature maps. In *Proceedings of the 19th ACM SIGKDD International Conference on Knowledge Discovery and Data Mining*, pages 239–247. ACM, 2013. 4
- [53] AJ Piergiovanni, Anelia Angelova, Alexander Toshev, and Michael S. Ryoo. Evolving space-time neural architectures for videos. In *The IEEE International Conference on Computer Vision (ICCV)*, October 2019. 8
- [54] Joseph Redmon, Santosh Divvala, Ross Girshick, and Ali Farhadi. You only look once: Unified, real-time object detection. *CVPR*, 2015. 3
- [55] Shaoqing Ren, Kaiming He, Ross Girshick, and Jian Sun. Faster R-CNN: Towards real-time object detection with region proposal networks. In *NIPS*, pages 91–99, 2015. 2, 3, 7
- [56] Jérôme Revaud, Philippe Weinzaepfel, Zaid Harchaoui, and Cordelia Schmid. EpicFlow: Edge-Preserving Interpolation of Correspondences for Optical Flow. In *CVPR*, 2015. 3
- [57] Marcus Rohrbach, Sikandar Amin, Mykhaylo Andriluka, and Bernt Schiele. A database for fine grained activity detection of cooking activities. In *CVPR*, 2012. 7
- [58] Olga Russakovsky, Jia Deng, Hao Su, Jonathan Krause, Sanjeev Satheesh, Sean Ma, Zhiheng Huang, Andrej Karpathy, Aditya Khosla, Michael Bernstein, Alexander C. Berg, and Li Fei-Fei. ImageNet large scale visual recognition challenge. *IJCV*, 115(3):211–252, 2015. 2, 3
- [59] Michael S. Ryoo, AJ Piergiovanni, Mingxing Tan, and Anelia Angelova. Assemblenet: Searching for multi-stream neural connectivity in video architectures. In *CoRR*, volume abs/905.13209v1, 2019. 9
- [60] Paul Scovanner, Saad Ali, and Mubarak Shah. A 3-Dimensional SIFT Descriptor and its Application to Action Recognition. *CRCV*, pages 1–4, 2007. 1, 3
- [61] Gunnar A. Sigurdsson, Gül Varol, Xiaolong Wang, Ali Farhadi, Ivan Laptev, and Abhinav Gupta. Hollywood in homes: Crowdsourcing data collection for activity understanding. In *ECCV*, 2016. 7
- [62] Karen Simonyan and Andrew Zisserman. Two-stream convolutional networks for action recognition in videos. In *NIPS*, pages 568–576, 2014. 1, 3
- [63] Josef Sivic and Andrew Zisserman. Video Google: A text retrieval approach to object matching in videos. *ICCV*, 2:1470–1477, 2003. 1, 3
- [64] Christian Szegedy, Sergey Ioffe, Vincent Vanhoucke, and Alexander A. Alemi. Inception-v4, inception-resnet and the impact of residual connections on learning. In *Proceedings of the Thirty-First AAAI Conference on Artificial Intelligence*, AAAI’17, pages 4278–4284. AAAI Press, 2017. 2, 3
- [65] Christian Szegedy, Vincent Vanhoucke, Sergey Ioffe, Jon Shlens, and Zbigniew Wojna. Rethinking the inception architecture for computer vision. In *The IEEE Conference on Computer Vision and Pattern Recognition (CVPR)*, June 2016. 2, 3
- [66] Yongyi Tang, Lin Ma, and Lianqiang Zhou. Hallucinating optical flow features for video classification. In *IJCAI*, 2019. 1
- [67] Du Tran, Lubomir Bourdev, Rob Fergus, Lorenzo Torresani, and Manohar Paluri. Learning Spatiotemporal Features with 3D Convolutional Networks. *ICCV*, pages 4489–4497, 2015. 1, 3
- [68] Jasper R.R. Uijlings, Ionut Cosmin Duta, Negar Rostamzadeh, and Nicu Sebe. Realtime Video Classification using Dense HOF/HOG. *ICMR*, 2014. 3
- [69] Jan C. van Gemert, Cor J. Veenman, Arnold W. M. Smeulders, and Jan-Mark Geusebroek. Visual word ambiguity. *TPAMI*, 32(7):1271–1283, July 2010. 3
- [70] Gül Varol, Ivan Laptev, and Cordelia Schmid. Long-term temporal convolutions for action recognition. *TPAMI*, 40(6):1510–1517, 2018. 3
- [71] Heng Wang, Alexander Kläser, Cordelia Schmid, and Liu Cheng-Lin. Action Recognition by Dense Trajectories. *CVPR*, pages 3169–3176, 2011. 1, 3
- [72] Heng Wang, Alexander Kläser, Cordelia Schmid, and Cheng-Lin Liu. Dense Trajectories and Motion Boundary Descriptors for Action Recognition. *IJCV*, 2013. 1, 3
- [73] Heng Wang and Cordelia Schmid. Action Recognition with Improved Trajectories. *ICCV*, pages 3551–3558, 2013. 1, 3
- [74] Jue Wang and Anoop Cheria. Learning discriminative video representations using adversarial perturbations. In *ECCV*, pages 716–733, 2018. 1, 2, 3, 8
- [75] Lei Wang, Piotr Koniusz, and Du Q. Huynh. Hallucinating IDT descriptors and I3D optical flow features for action recognition with cnns. In *The IEEE International Conference on Computer Vision (ICCV)*, October 2019. 1, 2, 3, 4, 5, 6, 8, 9

- [76] L. Wang, L. Wang, H. Lu, P. Zhang, and X. Ruan. Saliency detection with recurrent fully convolutional networks. In *ECCV*, pages 825–841, 2016. [3](#)
- [77] Kilian Weinberger, Anirban Dasgupta, John Langford, Alex Smola, and Josh Attenberg. Feature hashing for large scale multitask learning. In *ICML*, pages 1113–1120, 2009. [4](#)
- [78] Philippe Weinzaepfel, Jérôme Revaud, Zaid Harchaoui, and Cordelia Schmid. DeepFlow: Large displacement optical flow with deep matching. In *ICCV*, 2013. [3](#)
- [79] Geert Willems, Tinne Tuytelaars, and Luc Van Gool. An efficient dense and scale-invariant spatio-temporal interest point detector. In *ECCV*, pages 650–663, 2008. [3](#)
- [80] An Yan, Yali Wang, Zhifeng Li, and Yu Qiao. PA3D: Pose-action 3D machine for video recognition. In *The IEEE Conference on Computer Vision and Pattern Recognition (CVPR)*, June 2019. [8](#)
- [81] Lahav Yeffet and Lior Wolf. Local trinary patterns for human action recognition. *ICCV*, pages 492–497, 2009. [3](#)
- [82] Hongguang Zhang, Jing Zhang, and Piotr Koniusz. Few-shot learning via saliency-guided hallucination of samples. In *The IEEE Conference on Computer Vision and Pattern Recognition (CVPR)*, June 2019. [2](#), [3](#)
- [83] Jing Zhang, Tong Zhang, Yuchao Dai, Mehrtash Harandi, and Richard Hartley. Deep unsupervised saliency detection: A multiple noisy labeling perspective. In *The IEEE Conference on Computer Vision and Pattern Recognition (CVPR)*, June 2018. [2](#), [3](#)
- [84] W. Zhu, S. Liang, Y. Wei, and J. Sun. Saliency optimization from robust background detection. In *CVPR*, pages 2814–2821, 2014. [3](#)
- [85] Barret Zoph, Vijay Vasudevan, Jonathon Shlens, and Quoc V. Le. Learning transferable architectures for scalable image recognition. In *The IEEE Conference on Computer Vision and Pattern Recognition (CVPR)*, June 2018. [2](#), [3](#)